Wavelength-selective synaptic devices based on Graphdiyne/WSe2 for multi-color image recognition and neuromorphic computing

Tang, Hongyu; Shi, Weiqi; Jiang, Wanlin; Wang, Gaoyuan; Tang, Mengyuan; Cai, Zihao; Li, Ruiteng; Wu, Shuai; Zhang, Guoqi; Li, Jian

DOI
10.1016/j.cej.2025.164215

Publication date
2025

Document Version
Final published version

Published in
Chemical Engineering Journal

Chemical Engineering Journal 517 (2025) 164215

Contents lists available at ScienceDirect

Chemical Engineering Journal

journal homepage: www.elsevier.com/locate/cej

Wavelength-selective synaptic devices based on Graphdiyne/WSe_2 for multi-color image recognition and neuromorphic computing

Hongyu Tang [a,*], Weiqi Shi [a], Wanlin Jiang [b], Gaoyuan Wang [a], Mengyuan Tang [a], Zihao Cai [a], Ruiteng Li [c], Shuai Wu [c], Guoqi Zhang [d], Jian Li [e,f,*]

[a] Academy for Engineering & Technology, Fudan University, Shanghai 200433, China
[b] School of Microelectronics, Fudan University, Shanghai 200433, China
[c] School of Mechanical Engineering, Hebei University of Technology, Tianjin 300401, China
[d] EEMCS Faculty, Delft University of Technology, Delft 2628CD, the Netherlands
[e] Gongshu Institute of Future Technology, ZJUT, Hangzhou 310022, PR China
[f] Department of Physics, Zhejiang University of Technology, Hangzhou 310023, China

ARTICLE INFO

Keywords:
GDY NWs/WSe_2 heterostructures
Self-powered optoelectronic synapses
Wavelength-dependent reservoir
Multi-color image sensing
Neuromorphic image recognition

ABSTRACT

Graphdiyne (GDY)/two-dimensional materials (2DMs) heterostructures present unique opportunities for advanced optoelectronic and neuromorphic devices because of their exceptional electrical, optical, and structural properties. However, the traditional methods for construction of GDY/2DMs heterostructures usually lead to inferior interfaces, which seriously affects the charge separation and transport. Herein, an *in situ* approach for growing GDY nanowalls (NWs) on WSe_2 is employed in this work. The as-prepared GDY NWs/WSe_2 heterostructure exhibits self-powered broadband photodetection across 405–980 nm with a high responsivity of 2176 A/W and detectivity of 3.6×10^{12} Jones at 532 nm under 0.02 mW/cm^2 illumination, significantly outperforming previously reported GDY-based devices. The efficient charge separation and strong photocarrier trapping in the GDY NWs/WSe_2 heterostructure result in pronounced short-term and long-term synaptic plasticity. The nonlinear, wavelength-dependent reservoir state separation enables clear distinction of multiple pulse sequences, which shows great potential for logic processing. The successfully resolved red, green, and violet patterns, and one-shot color image recognition of a 5-letter image highlight transformative potential of GDY NWs/WSe_2 device for future adaptive imaging and neuromorphic computing technologies.

1. Introduction

Vast amounts of data generated in Artificial Intelligence drive demand for high-performance memory and processor devices [1]. Traditional Von Neumann computers are limited by restricted computational speed and increased energy consumption due to the physical separation between processing and memory units [2,3]. Neuromorphic computing, inspired by the human brain, provides notable benefits in tasks involving complex learning, recognition, perception, and memory. These include superior fault tolerance, rapid computation, and extremely low power consumption [4–7]. Optical synaptic devices that merge optical signal sensing with synaptic capabilities in one unit are particularly attractive for neuromorphic systems [8,9].

Two-dimensional materials (2DMs) with ultrathin structures and highly tunable optoelectronic properties have shown great potential in optoelectronic neuromorphic devices [10–14]. To further amplify the synaptic response, 2DMs-based heterostructures have been widely constructed to improve light absorption and enhance carrier trapping capability at the heterogeneous interface [15–17]. Owing to the highly π-conjugated structure [18–20], uniformly distributed pores [21], abundant charge trapping sites [22], high carrier mobility [23], tunable direct bandgap [24], and remarkable mechanical flexibility [25], graphdiyne (GDY) has enabled the development of novel synaptic and memory devices based on GDY/ZnO [26], GDY/TiO_2 [27], MoS_2/GDY [28], graphene/GDY [29], Pyr-GDY/graphene/PbS quantum dots (QDs) [30], GDY/GDY QDs [31] heterostructures, *etc*. GDY serves as light absorber layers, charge trapping layers, or ion storage layers in these devices [1]. However, the preparation of 2DMs/GDY is still limited to the orderly and quantitative deposition of GDY on the surface of metal foils via chemical vapor deposition, followed by wet transfer onto 2D

* Corresponding authors.
E-mail addresses: hongyu_tang@fudan.edu.cn (H. Tang), jian.li@hzgift.org (J. Li).

https://doi.org/10.1016/j.cej.2025.164215
Received 20 February 2025; Received in revised form 26 May 2025; Accepted 26 May 2025
Available online 1 June 2025

material surfaces [32]. The processes inevitably introduce defects and folds, adversely impacting the charge transport of the heterostructures. Compared to the planar type of GDY, GDY nanowalls (NWs) with a high surface area can significantly enhance charge transfer, light absorption, and photogenerated carrier capture. Tungsten diselenide (WSe_2) with an indirect bandgap of ~ 1.2 eV has bipolar transport behaviours [33]. The high carrier mobility and superior optical properties endow the WSe_2 based photodetector with a photoresponsivity of 10^{-1} to 10^5 A/W in the visible range [34–36]. However, the study on 2DMs/GDY NWs heterojunctions is elusive [37,38].

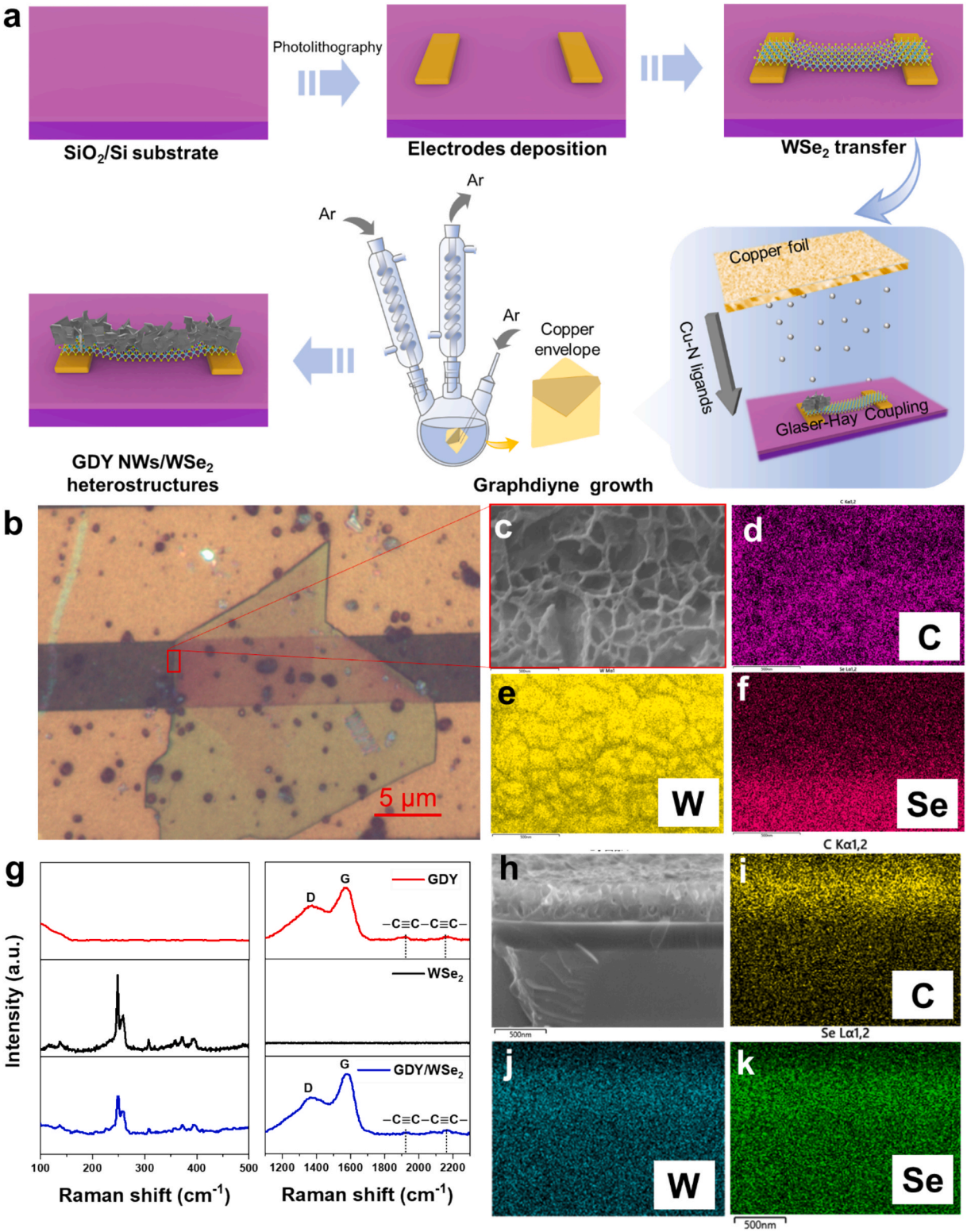

Fig. 1. Characterization of as-fabricated GDY/WSe_2 heterostructures. (a) Synthesis of GDY NWs on WSe_2 above SiO_2/Si substrates via copper envelope catalysis. (b) Optical image of GDY/WSe_2 heterostructures. (c) SEM images of GDY/WSe_2. (d-f) Elemental mapping of carbon (C), tungsten (W) and selenium (Se) by EDS. (g) Raman of intrinsic GDY, WSe_2, and GDY/WSe_2 heterostructure; (h) Cross-sectional SEM images of GDY/WSe_2. (i-k) Elemental mapping of C, W and Se by EDS.

With this in mind, GDY NWs were *in situ* grown on WSe_2 surface to form GDY NWs/WSe_2 heterostructure. The device exhibits exceptional self-powered photodetection performance across a wide wavelength range from 405 nm to 980 nm, achieving a high photodetection responsivity of 2176 A/W and detectivity of 3.6×10^{12} Jones under green light. The retinomorphic device exhibits stable photoresponsivities across the red, green, and violet spectra, positioning it as a promising candidate for in-sensor 4-bit encoding and the processing of images via convolutional neural networks (CNNs). A configurable CNN with diverse convolution kernels is successfully implemented for multicolor image processing tasks with 100 % classification accuracy for colored letters. This accomplishment highlights the potential of *in-situ* construction of GDY heterostructures for in-sensor computing, offering new perspectives for developing neuromorphic vision sensors tailored for diverse applications.

2. Results and discussion

2.1. GDY/WSe_2 Characterization

Fig. 1a illustrates the preparation process of the GDY NWs/WSe_2 heterostructure devices using a copper-encapsulation catalytic strategy. In brief, mechanically exfoliated WSe_2 on pre-patterned electrodes was wrapped in copper foil and immersed in a solution containing pyridine, acetone, hexaethynylbenzene (HEB), and N,N,N′,N′-tetramethylethylenediamine (TMEDA) [37]. After heating at 50 °C for 12 h, the GDY NWs/WSe_2 heterostructure was prepared on the target substrate. The morphology of GDY NWs/WSe_2 was characterized using optical microscopy (Fig. 1b) and scanning electron microscopy (SEM) (Fig. 1c). SEM images from the red-box inset in Fig. 1b are shown in Fig. 1c-f and Fig. S1. 3D honeycomb-shaped GDY is clearly observed on the WSe_2 surface. The corresponding energy dispersive spectroscopy (EDS) elemental mapping confirms the uniform distribution of carbon (C) across tungsten (W) and selenium (Se) region. Cross-sectional SEM images (Fig. 1h-k) reveal the solid interface between GDY NWs (~300 nm thickness) and WSe_2. Atomic force microscopy (AFM) determines that the thickness of WSe_2 is 60 nm (Fig. S2). The details of device fabrication methods and characterizations are provided in the Note 1 and Note 2 of supporting information. Raman spectroscopy was employed to explore interlayer coupling in the GDY/WSe_2 heterostructure (Fig. 1g). Two Raman peaks at 248 cm^{-1} and 258.3 cm^{-1} are observed for WSe_2. Four significant peaks at 1378.2, 1573.8, 1930.6, and 2180.7 cm^{-1} in GDY are aligned with previously reported values [39]. For the GDY/WSe_2 heterostructure, the D, G, and diacetylene peaks located at 1377.8, 1580.8, 1932.6, and 2171.5 cm^{-1} reveal the characteristics of GDY. Two peaks at 248.2 cm^{-1} and 257.1 cm^{-1} with lower intensity, indicate that the WSe_2 is underneath GDY. The slight shift in the WSe_2 peak confirmed the formation of high-quality heterointerfaces.

2.2. Optoelectronic characterizations

The current–voltage (I_{ds}-V_{ds}) characteristics of GDY, WSe_2 and GDY/WSe_2 were measured under dark and illuminated conditions (Fig. 2b, c). Unlike pristine GDY NWs with no significant response, the increased current in WSe_2 and GDY/WSe_2 heterostructures exhibit a photovoltaic (PV) effect and a high light-to-dark current ratio of 10^3 at $V_{ds} = 0$ V. To further measure the detection range, the device was tested under 1 mW/cm^2 laser power density (P_{in}) at 405, 532, 635, 780, 880, and 980 nm. The upshift under illumination illustrates the self-powered broadband photodetection capability of GDY/WSe_2 (Fig. 2d). Notably, the heterostructure achieves an outstanding responsivity of 2176 A/W at $V_{ds} = 1$ V and $P_{in} \approx 0.02$ mW/cm^2, significantly surpassing previously reported GDY-based photodetectors [40]. Because of the decreased scattering and recombination, the photoresponsivity (R) linearly declines with increasing P_{in} (Fig. 2e) [28]. The corresponding external quantum efficiency (EQE) and detectivity (D^*) are calculated to be 5.1×10^6% and

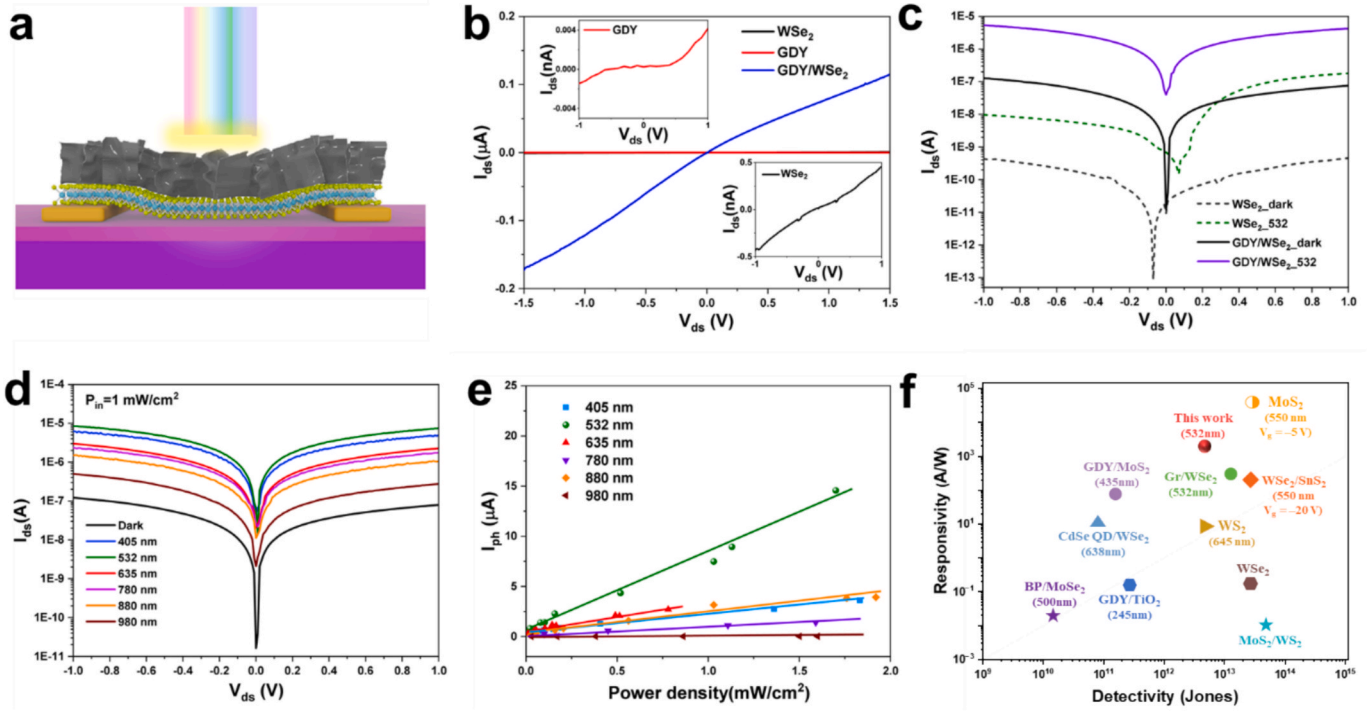

Fig. 2. Optoelectronic characteristics of the optical synapse based on the GDY/WSe_2 heterostructure. (a) Schematic diagram of GDY/WSe_2 device under illumination; (b) I_{ds}–V_{ds} curves of GDY, WSe_2 and GDY/WSe_2 under dark. (c) I_{ds}–V_{ds} curves of WSe_2 and GDY/WSe_2 under dark and 532 nm with laser power density (P_{in}) of 1 mW/cm^2. (d) I_{ds}–V_{ds} curves of GDY/WSe_2 in dark, and illuminated at 405, 532, 635, 780, 880, and 980 nm. (e) Wavelength-dependent photocurrent ranging from 405 to 980 nm at $V_{ds} = 1$ V at various laser power densities. (f) Comparison with previous reports based on GDY and TMDs photodetector in terms of responsivity and detectivity. Note: The detectivity and responsivity of MoS_2 and WSe_2/SnS_2 devices are tested with gate bias (V_g).

3.6×10^{12} Jones, at 0.02 mW/cm^2 (532 nm), the best values among the GDY-based heterojunctions (Table S1, Note 3, Supporting information). Compared to GDY-based and 2DMs-based devices, the GDY/WSe_2 heterostructure exhibits simultaneous high responsivity, detectivity, and EQE at low V_{ds} without gate bias modulations (Fig. 2f).

We further explore the device's potential in simulating optical synaptic activities. As shown in Fig. 3a, applying a presynaptic optical signal generates a postsynaptic current (PSC, I_{ds}), mimicking both long-term and short-term synaptic plasticity. After the light pulse ceases, the current gradually stabilizes (Fig. 3b). Under a 50 ms optical pulse, the device shows a sharp current rise due to photogenerated carrier accumulation, followed by slow decay and prolonged relaxation time, indicating the short-term potentiation (STP) behavior [41]. The PSC increases significantly and stabilizes at an elevated level over time, marking the transition from STP to long-term potentiation (LTP). With continuous light input (i.e. 1, 5, 20 and 50 pulses), the PSC continues to

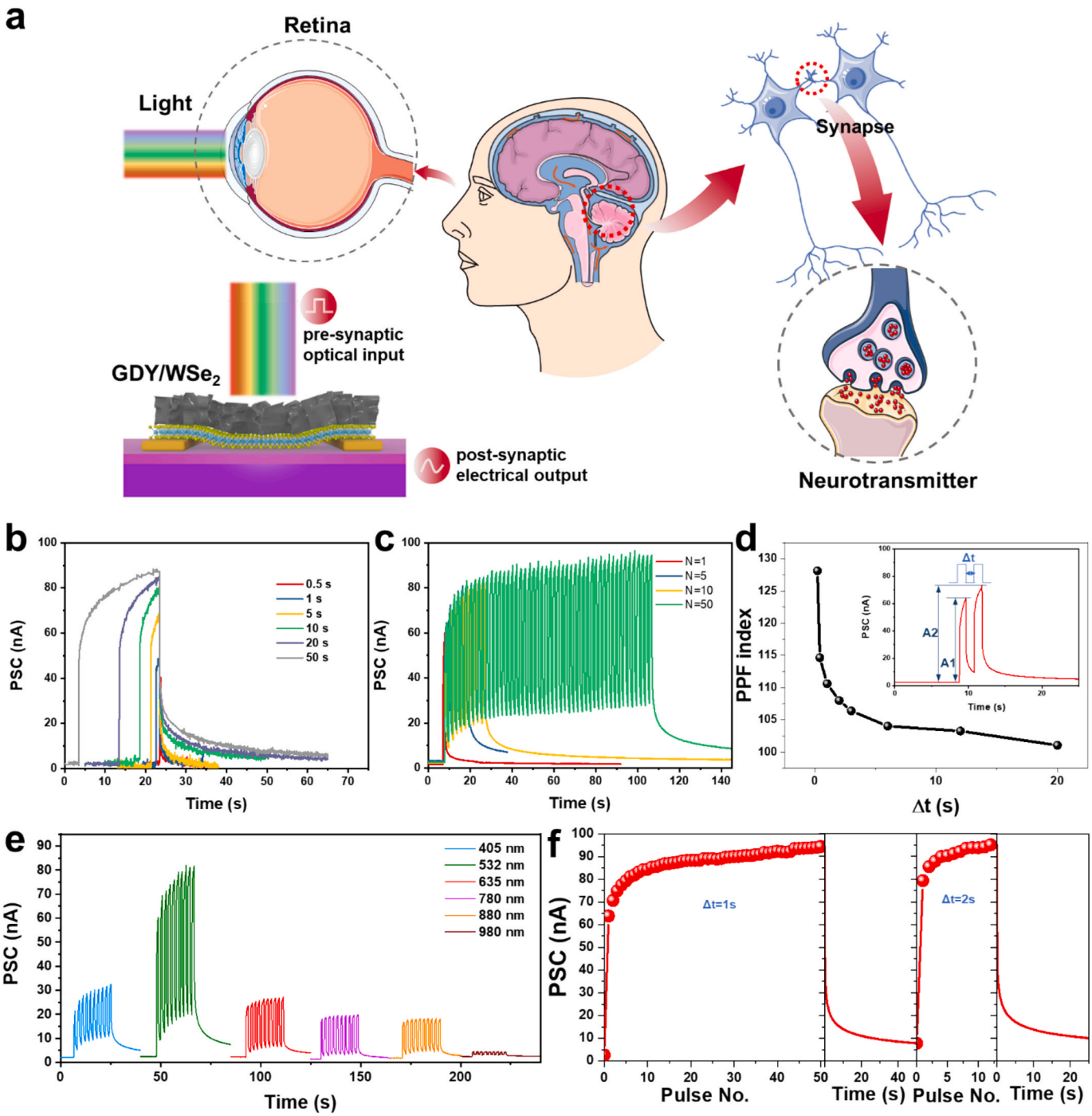

Fig. 3. Optical synaptic characteristics achieved by GDY/WSe_2 heterostructure devices. (a) Configuration illustration GDY/WSe_2 optoelectronic synapse, and brain-like visual perception and information transmission. (b) The current response to light pulses of varying durations (532 nm, 1 mW/cm^2). (c) Current response induced by 1, 5, 10, and 50 light pulses (532 nm, 1 mW/cm^2, 1 s). (d) The PPF index versus the pulse interval (Δt) for PSC. The inset indicates the PSC induced by two consecutive light pulses. (e) PSC response of GDY/WSe_2 heterostructure devices to light pulses at 405, 532, 635, 780, 880 and 980 nm wavelengths (1 mW/cm^2, 1 s). (f) PSC changes in the memory process. Parts of the figure were drawn using Servier Medical Art licensed under a Creative Commons Attribution 3.0 Unported License (https://creativecommons.org/licenses/by/3.0/).

rise, facilitating the transition (Fig. 3c). The transition is driven by carrier migration from shallow to deep traps [42,43]. This mechanism resembles biological synapses where sustained stimulation releases more neurotransmitters [44]. The paired-pulse facilitation (PPF) index decreases exponentially with increasing time intervals (Δt) (Fig. 3d), reflecting the dynamic filtering properties of biological synapses during information transmission. The highest synaptic response occurs at 532 nm, consistent with the previous photocurrent-wavelength trends (Fig. 3e). It is noted that our device enters a deep trap state under all three laser types, with synaptic responses influenced by trap center density. Therefore, the device shows decent synaptic response at 405 nm laser despite low absorption.

To evaluate the memory properties, a "learning-forgetting-relearning" test was conducted to simulate human memory processes (Fig. 3f). After 50 pulses, synaptic weight gradually increases but decays upon stimulation removal, indicating spontaneous forgetting of the post-synaptic current. Upon a second stimulation (2 s interval), only 10 pulses restore the original current level, exhibiting slower post-stimulus decay. This phenomenon parallels the cognitive process wherein humans require less time to relearn forgotten information, and such relearning significantly enhances memory stability. Furthermore, we irradiated under 532 nm laser at 1.17 μW/cm^2 for 40 h to investigate the operation stability of the device (Fig. S3). As demonstrated in Note 4 of Supporting information, the device takes around 8 h to recover to the initial state. The post-storage analysis after several months reveals no significant degradation in device response, and the structure of the device is not found to be delaminated after dissecting the device, thereby validating robust long-term storage reliability. Consequently, the GDY/WSe_2 heterostructure integrates light-sensing, memory functionalities, and practical applicability, thereby demonstrating suitability for neuromorphic vision systems.

2.3. Mechanisms analysis

To gain deeper insight into the charge separation in the GDY/WSe_2 heterostructure, first-principles analysis was conducted (Fig. 4a). Detailed calculations are provided in Note 5 and Fig. S4 of the supporting information. As shown in Fig. 4b and Fig. S4, the significant charge transfer from WSe_2 to GDY establishes a built-in potential, aligning with the type-II band diagram of GDY/WSe_2 (Fig. 4c) as confirmed by Kelvin probe force microscopy (KPFM) (Fig. S5 and Note 6 in Supporting information). The higher Fermi level (E_f) of WSe_2 drives electron diffusion into GDY, where defects trap carriers. The GDY NWs exhibit a high absorption coefficient at 532 nm, which is the main factor contributing to their peak photoresponsivity observed at this wavelength (Fig. 4d) [45,46]. The type-II band alignment in Fig. 4c promotes photogenerated carrier separation upon light pulse illumination. Thus, numerous excited electrons transferred from the conduction band of WSe_2 into GDY, while the built-in electric field at the GDY/WSe_2 interface simultaneously drives holes from GDY's valence band into WSe_2 (Fig. 4e). The conjugated π structures and C-O and C=O bonds on the edges of GDY (Fig. S6) enable mutual charge trapping [26,40,47]. Electrons accumulate in GDY while holes reside in WSe_2, effectively slowing electron-hole recombination (Fig. 4f). Consequently, the GDY/WSe_2 heterojunction exhibits optoelectronic synaptic plasticity.

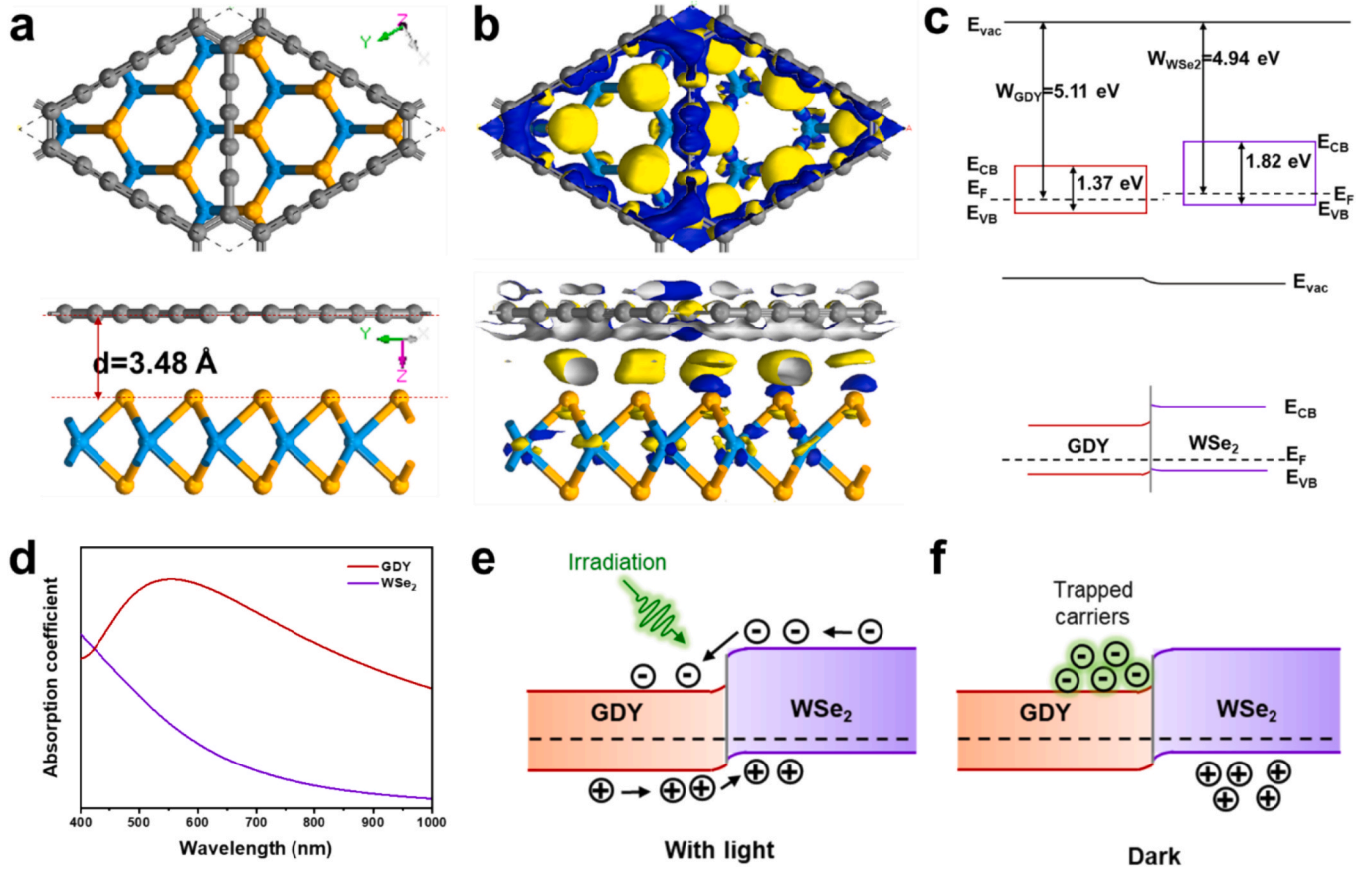

Fig. 4. Mechanism of the optoelectronic synaptic behavior in GDY/WSe_2 heterojunction. (a) Top and side view of GDY/WSe_2. The W, Se, and C atoms are depicted in blue, yellow, and gray, respectively. (b) The charge density difference at GDY/WSe_2 interface, where the blue and yellow isosurfaces represent negative and positive charge densities, respectively. (c) Band diagram of GDY and WSe_2 before and after the contacts. (d) The adsorption coefficient of the GDY and WSe_2. Band alignment of the GDY/WSe_2 heterojunction (e) with light irradiation, and (f) with light off.

2.4. Adaptive temporal specificity and image sensing

Time-input responses were further examined using 4-bit pulse sequences to investigate the GDY NWs/WSe_2-based device's adaptive temporal specificity. Four consecutive pulses with varying trigger voltages were applied within each pulse period, with trigger-off (dark) and trigger-on (532 nm) states denoted as "0″ and "1″, respectively, generating 16 distinct pulse sequences. The distinct reservoir states indicate that laser wavelength modulation enables a broader and adjustable state range (Fig. 5a). The 16 distinct current outputs at varying wavelengths exhibit minimal overlap, demonstrating wavelength-dependent reservoir state generation (Fig. 5b). The transient photocurrent analysis in Fig. S7 reveals that the decay time at 635 nm, 780 nm, and 980 nm is within 1 s, suggesting the carriers occupy shallow trap states. In contrast, LTP under 405 and 532 nm irradiation is attributed to enhanced photogenerated carrier migration from shallow to deep traps. [48] The clear separation of inputs suggests that temporal signals are nonlinearly mapped to reservoir states, which enhances the potential for further time-pulse sequence training and recognition (Fig. S8). This phenomenon stems from wavelength-dependent photogenerated carrier dynamics, including absorption coefficient, absorption depth, carrier generation, and recombination mechanisms, accumulating at trap centers and driving different reservoir dynamics. Such adaptive temporal characteristics enable the device to generate more output signals, effectively separating and expanding storage states for each time input.

A prototype visible-light imager utilizing a GDY NWs/WSe_2 device as an imaging pixel was demonstrated in Fig. 5c. A three-primary-color laser source illuminated a shadow mask engraved with letters "FDU". The device, mounted on a dual-axis XY precision displacement platform, scanned the image along x and y axes at 3.38 Hz (0.296 s/period). The multi-color images of "F" (red, 635 nm), "D" (green, 532 nm), and "U" (violet, 405 nm) were clearly observed in Fig. 5d. This single-pixel imager offers potential for multi-pixel imaging. Future integration with array fabrication and color-processing algorithms could enable full-color array sensors mimicking conventional cameras.

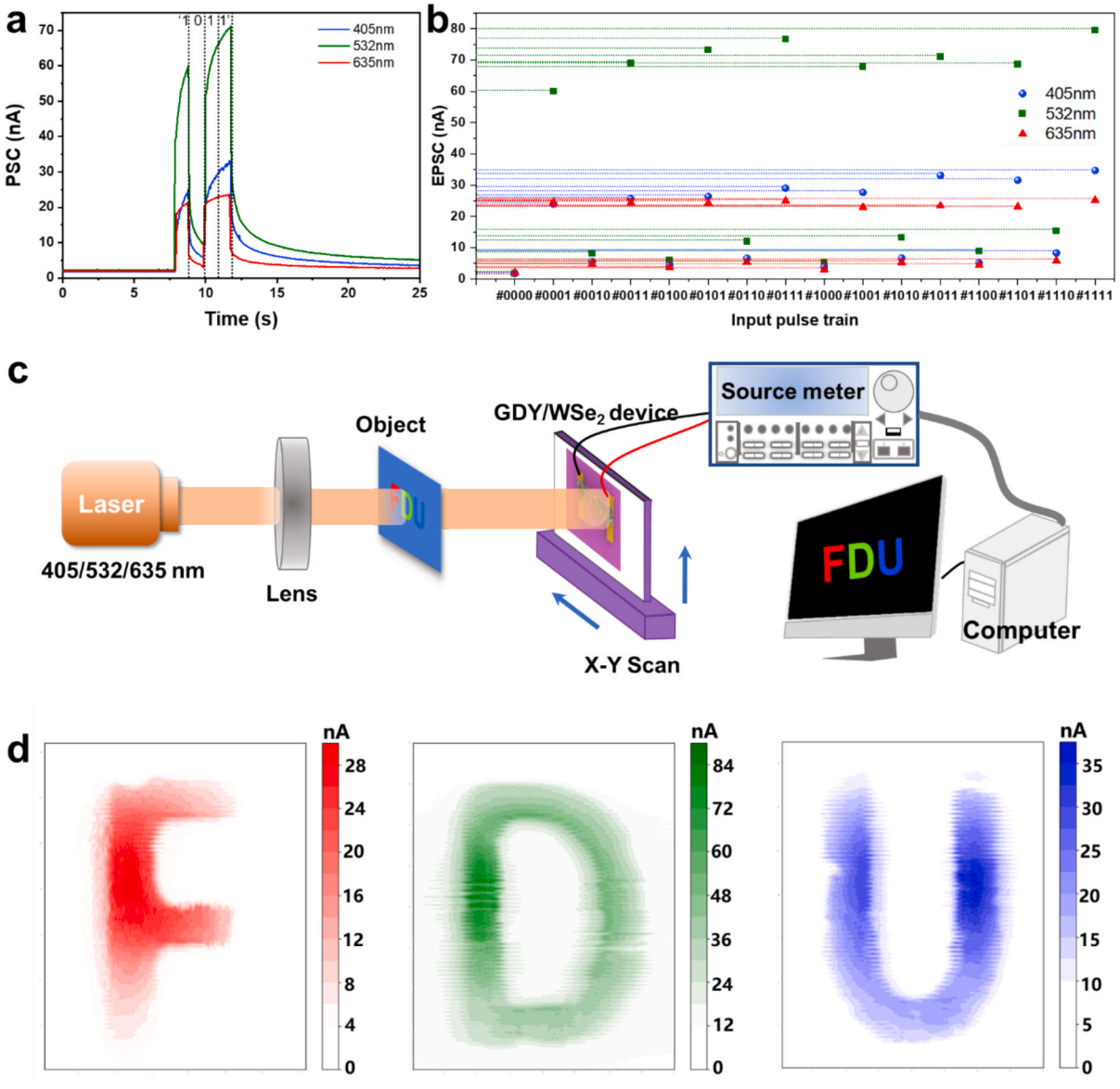

Fig. 5. Adaptive temporal specificity and image sensing of the GDY NWs/WSe_2 devices. (a) A typical pulse sequence of "1011" under different wavelength (V_{ds} = 0.01 V, P_{in} = 1 mW/cm^2). (b) The EPSC responses to 16 different pulse trains for 4-bit separation and multiple reservoir states (Δt = 1 s, V_{ds} = 0.01 V, P_{in} = 1 mW/cm^2). (c) A schematic of the image scanning system, featuring three different light sources: red, green, and violet. (d) Corresponding image obtained by scanning the 'FDU' images with a single-pixel imager based on the GDY NWs/WSe_2.

2.5. Image recognition capability

To evaluate its practical applications, the image recognition capability is investigated. A CNN classifier, composed of a 5-channel convolutional layer and activation layers, is constructed for multi-letter image recognition based on the I_{ph}-P_{in} curve under 405 nm (violet), 532 nm (green) and 635 nm (red) illumination. The number of channels in the convolutional layer corresponds to the number of input images, with each channel containing a kernel that extracts features from the input image. A sigmoid function with a scaling factor is employed as the activation function to ensure full value range accessibility during training during training. The dataset for training and testing comprises 15 letters, 'F', 'U', 'D', 'A' and 'N' in violet, green and red, represented as 3-channel images. The training dataset is expanded to 250 samples incorporating five Gaussian noise levels (Fig. 6a), while the testing dataset remains at 50 samples with level-1 noise. After 50 training epochs, the 15 images are used to train weights in corresponding kernels (Fig. 6b), followed by multi-channel processing to determine maximum recognition probability (Fig. 6c) of image recognition. Fig. S9 illustrates the CNN's training loss and accuracy under varying artificial noise levels. Consequently, the five letters in three colors are successfully classified, demonstrating the high-accuracy image recognition capability of the GDY NWs/WSe_2 device. Detailed calculations are provided in Note 7 of the supporting information.

3. Conclusions

In summary, this study demonstrates the *in situ* synthesis of GDY NWs/WSe_2 heterostructures with remarkable optoelectronic and neuromorphic computing capabilities. The heterostructures deliver self-powered broadband photodetection from UV to NIR spectrum (405–980 nm) and achieve an exceptional responsivity of 2176 A/W and detectivity of 3.6×10^{12} Jones under green light at low power densities, surpassing previously reported GDY-based devices. The GDY NWs/WSe_2 devices mimic synaptic plasticity through short/long-term memory behaviors, essential for neuromorphic systems. The retinomorphic device exhibits stable photoresponse across red (635 nm), green (532 nm), and violet (405 nm) spectra, enabling in-sensor 4-bit encoding and multi-color image sensing. By implementing a configurable CNN with diverse convolution kernels, we achieve 100 % accuracy in classifying the 5 letters 'F', 'U', 'D', 'A', and 'N' in three colors, demonstrating the high-accuracy image recognition capability of the GDY NWs/WSe_2 device. The wavelength-dependent reservoir state dynamics enable effective separation and processing of spatio-temporal signals, facilitating advanced tasks like and artificial neural network-based image recognition. With their superior photodetection, adaptive learning, and image sensing capabilities, these devices hold significant potential for future applications in neuromorphic computing, intelligent imaging, and wavelength-selective photodetection technologies.

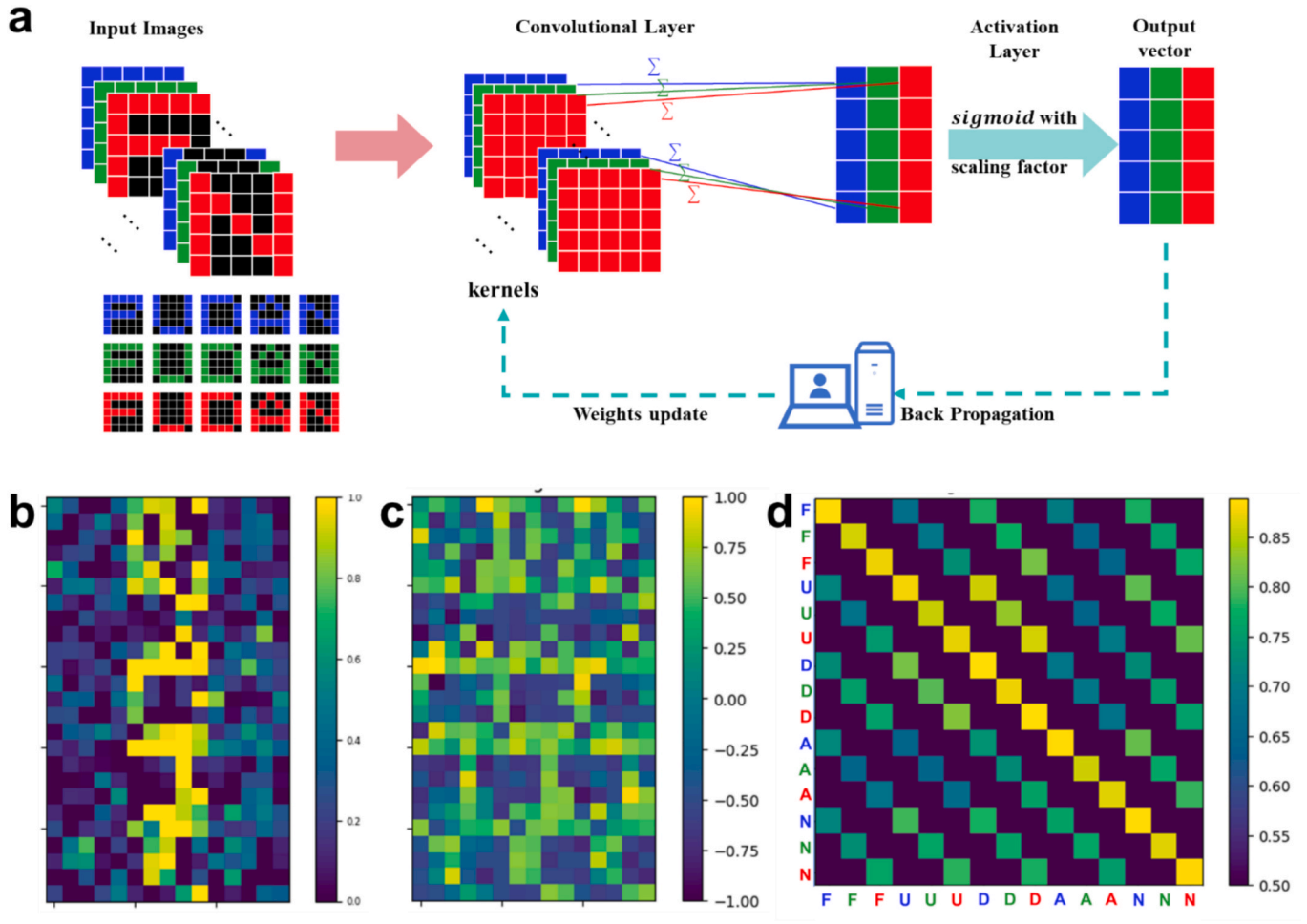

Fig. 6. One-shot recognition of multi-letter image based on CNN under 405 nm (violet), 532 nm (green) and 635 nm (red) illumination. (a) The training process of image recognition for 15 target letters "FUDAN". (b) Data matrix of 5 letter images (noise level2). (c) Trained weight matrix (noise level2). (d) One-shot recognition of 15 letter images.

CRediT authorship contribution statement

Hongyu Tang: Writing – original draft, Validation, Methodology, Formal analysis, Data curation, Conceptualization. **Weiqi Shi:** Visualization, Data curation. **Wanlin Jiang:** Validation, Methodology, Data curation. **Gaoyuan Wang:** Validation, Data curation. **Mengyuan Tang:** Visualization, Formal analysis. **Zihao Cai:** Data curation. **Ruiteng Li:** Data curation. **Shuai Wu:** Supervision, Investigation. **Guoqi Zhang:** Writing – review & editing, Supervision. **Jian Li:** Writing – review & editing, Validation, Supervision, Methodology, Data curation.

Declaration of competing interest

The authors declare that they have no known competing financial interests or personal relationships that could have appeared to influence the work reported in this paper.

Acknowledgment

This work was supported by FDUROP (Fudan Undergraduate Research Opportunities Program) (Grant No.24085), Shanghai Research Center for Silicon Carbide Power Devices Engineering &Technology Project [Grant No. 19DZ2253400] and ZJUT Research Program (YJY-ZS-20240001).

Appendix A. Supplementary data

Supplementary data to this article can be found online at https://doi.org/10.1016/j.cej.2025.164215.

Data availability

Data will be made available on request.

References

[1] Z.C. Zhang, X.D. Chen, T.B. Lu, Recent progress in neuromorphic and memory devices based on graphdiyne, Sci Technol Adv Mat 24 (2023).
[2] I. Mondal, R. Attri, T.S. Rao, B. Yadav, G.U. Kulkarni, Recent trends in neuromorphic systems for non-von Neumann computing and cognitive functionalities, Appl Phys Rev 11 (2024).
[3] B.J. Copeland, Z. Fan, Turing and Von Neumann: From Logic to the Computer, Philosophies 8 (2023).
[4] G.D. Zhou, Z.R. Wang, B. Sun, F.C. Zhou, L.F. Sun, H.B. Zhao, X.F. Hu, X.Y. Peng, J. Yan, H.M. Wang, W.H. Wang, J. Li, B.T. Yan, D.L. Kuang, Y.C. Wang, L.D. Wang, S.K. Duan, Volatile and Nonvolatile Memristive Devices for Neuromorphic Computing, Adv Electron Mater 8 (2022).
[5] S.J. Liang, Y.X. Li, B. Cheng, F. Miao, Emerging Low-Dimensional Heterostructure Devices for Neuromorphic Computing, Small Struct 3 (2022).
[6] H.L. Li, X.T. Jiang, W.B. Ye, H. Zhang, L. Zhou, F. Zhang, D.H. She, Y. Zhou, S. T. Han, Fully photon modulated heterostructure for neuromorphic computing, Nano Energy 65 (2019).
[7] Z.H. Shen, Z.X. Yang, Y.Q. Zhou, Y.L. Ye, B.Q. Ye, Q.C. Huang, W.B. Wu, H. Y. Hong, Z.Q. Hong, Z.Y. Meng, Z.W. Zeng, S.W. Ye, Z.M. Cheng, Q.T. Lan, J. X. Wang, Y. Chen, H. Zhang, T.L. Guo, Y. Ye, Z.Z. Weng, Y.Y. Chen, Ultralow-power consumption photonic synapse transistors based on organic array films fabricated using a particular prepatterned-guided crystallizing strategy, J Mater Chem C 11 (2023) 3213–3226.
[8] C.H. Kai, Y. Wang, X.P. Liu, X. Liu, X.Q. Zhang, X.D. Pi, D.R. Yang, AlGaN/GaN-Based Optoelectronic Synaptic Devices for Neuromorphic Computing, Adv, Opt Mater (2023).
[9] L.-F. Shen, L.-X. Hu, F.-W. Kang, Y.-M. Ye, F. Zhuge, Optoelectronic neuromorphic devices and their applications, Acta Phys. Sin. 71 (2022) 148505–148501.
[10] A. Wali, S. Das, Two-Dimensional Memtransistors for Non-Von Neumann Computing: Progress and Challenges, Adv Funct Mater 34 (2024).
[11] J.X. Chen, W.T. Xu, 2D-materials-based optoelectronic synapses for neuromorphic applications, Escience 3 (2023).
[12] C.Z. Lv, F.Q. Zhang, C.Y. Li, Z.Y. Li, J. Zhao, Low-dimensional optoelectronic synaptic devices for neuromorphic vision sensors, Mater Futures 2 (2023).
[13] Z.R. Zhang, D.L. Yang, H.H. Li, C. Li, Z.R. Wang, L.F. Sun, H.J. Yang, 2D materials and van der Waals heterojunctions for neuromorphic computing, Neuromorph Comput En 2 (2022).
[14] X.W. Feng, X.K. Liu, K.W. Ang, 2D photonic memristor beyond graphene: progress and prospects, Nanophotonics-Berlin 9 (2020) 1579–1599.
[15] Y. Zhang, P. Huang, J. Guo, R.C. Shi, W.C. Huang, Z. Shi, L.M. Wu, F. Zhang, L. F. Gao, C. Li, X.W. Zhang, J.L. Xu, H. Zhang, Graphdiyne-Based Flexible Photodetectors with High Responsivity and Detectivity, Adv Mater 32 (2020).
[16] Y. Li, M.J. Zhang, X.L. Hu, X.D. Li, R. Li, L.M. Yu, X.H. Fan, N.Y. Wang, C.S. Huang, Y.L. Li, Graphdiyne Visible-Light Photodetector with Ultrafast Detectivity, Adv Opt Mater 9 (2021).
[17] P.V. Pham, S.C. Bodepudi, K. Shehzad, Y. Liu, Y. Xu, B. Yu, X.F. Duan, 2D Heterostructures for Ubiquitous Electronics and Optoelectronics: Principles, Opportunities, and Challenges, Chem Rev 122 (2022) 6514–6613.
[18] X. Gao, H.B. Liu, D. Wang, J. Zhang, Graphdiyne: synthesis, properties, and applications, Chem. Soc. Rev. 48 (2019) 908–936.
[19] Y. Kong, J.Q. Li, S. Zeng, C. Yin, L.M. Tong, J. Zhang, Bridging the Gap between Reality and Ideality of Graphdiyne: The Advances of Synthetic Methodology, Chem-Us 6 (2020) 1933–1951.
[20] Y.J. Li, L. Xu, H.B. Liu, Y.L. Li, Graphdiyne and graphyne: from theoretical predictions to practical construction, Chem. Soc. Rev. 43 (2014) 2572–2586.
[21] H. Li, J.H. Lim, Y.P. Lv, N.N. Li, B.T. Kang, J.Y. Lee, Graphynes and Graphdiynes for Energy Storage and Catalytic Utilization: Theoretical Insights into Recent Advances, Chem Rev 123 (2023) 4795–4854.
[22] Q.Y. Zheng, G.F. Luo, Q.H. Liu, R. Quhe, J.X. Zheng, K.C. Tang, Z.X. Gao, S. Nagase, J. Lu, Structural and electronic properties of bilayer and trilayer graphdiyne, Nanoscale 4 (2012) 3990–3996.
[23] D.P. Do, E. Lee, V.Q. Bui, H. Lee, Recent progress in two-dimensional graphdiyne: Synthesis, characterization, and applications, ChemPhysMater 4 (2025) 91–107.
[24] Y. Li, Z.C. Zhang, J.Q. Li, X.D. Chen, Y. Kong, F.D. Wang, G.X. Zhang, T.B. Lu, J. Zhang, Low-voltage ultrafast nonvolatile memory via direct charge injection through a threshold resistive-switching layer, Nat Commun 13 (2022).
[25] J.Q. Li, Z.C. Zhang, Y. Kong, B.W. Yao, C. Yin, L.M. Tong, X.D. Chen, T.B. Lu, J. Zhang, Synthesis of wafer-scale ultrathin graphdiyne for flexible optoelectronic memory with over 256 storage levels, Chem-Us 7 (2021).
[26] Z.W. Jin, Q. Zhou, Y.H. Chen, P. Mao, H. Li, H.B. Liu, J.Z. Wang, Y.L. Li, Graphdiyne:ZnO Nanocomposites for High-Performance UV Photodetectors, Adv Mater 28 (2016) 3697–3702.
[27] Y. Li, D. Kuang, Y.F. Gao, J. Cheng, X.Y. Li, J. Guo, Z.N. Yu, Titania:Graphdiyne nanocomposites for high-performance deep ultraviolet photodetectors based on mixed-phase MgZnO, J Alloy Compd 825 (2020).
[28] D.P. Do, C.Y. Hong, V.Q. Bui, T.H. Pham, S. Seo, V.D. Do, T.L. Phan, K.M. Tran, S. Haldar, B.W. Ahn, S.C. Lim, W.J. Yu, S.G. Kim, J.H. Kim, H. Lee, Highly Efficient Van Der Waals Heterojunction on Graphdiyne toward the High-Performance Photodetector, Adv Sci 10 (2023).
[29] Z.C. Zhang, Y. Li, J.J. Wang, D.H. Qi, B.W. Yao, M.X. Yu, X.D. Chen, T.B. Lu, Synthesis of wafer-scale graphdiyne/graphene heterostructure for scalable neuromorphic computing and artificial visual systems, Nano Res 14 (2021) 4591–4600.
[30] Y.X. Hou, Y. Li, Z.C. Zhang, J.Q. Li, D.H. Qi, X.D. Chen, J.J. Wang, B.W. Yao, M. X. Yu, T.B. Lu, J. Zhang, Large-Scale and Flexible Optical Synapses for Neuromorphic Computing and Integrated Visible Information Sensing Memory Processing, ACS Nano 15 (2021) 1497–1508.
[31] Z. Ghafary, A. Salimi, R. Hallaj, K. Akhtari, F. Ghasemi, Light triggering performance of the van der Waals heterojunction of 2D/0D graphdiyne/graphdiyne quantum dot as a novel phototransistor, Carbon 215 (2023).
[32] C.S. Huang, Y.J. Li, N. Wang, Y.R. Xue, Z.C. Zuo, H.B. Liu, Y.L. Li, Progress in Research into 2D Graphdiyne-Based Materials, Chem Rev 118 (2018) 7744–7803.
[33] Q.L. Cheng, J.B. Pang, D.H. Sun, J.G. Wang, S. Zhang, F. Liu, Y.K. Chen, R.Q. Yang, N. Liang, X.H. Lu, Y.C. Ji, J. Wang, C.C. Zhang, Y.H. Sang, H. Liu, W.J. Zhou, WSe2 2D p-type semiconductor-based electronic devices for information technology: Design, preparation, and applications, InfoMat 2 (2020) 656–697.
[34] H. Shin, M. Taqi, F. Ali, S. Lee, M.S. Choi, C. Kim, B.H. Lee, X.C. Liu, J. Sun, B. Oh, W.J. Yoo, Self-Powered 2D MoS2/WOx/WSe2 Heterojunction Photodetector Realized by Oxygen Plasma Treatment, Adv Mater Interfaces 9 (2022).
[35] H.T. Meng, F. Zhang, Z.X. Mo, Q.L. Xia, M.A.Z. Zhong, J. He, Energy transfer in hybrid 0D-CdSe quantum dot/2D-WSe2 near-infrared photodetectors, J Phys D Appl Phys 55 (2022).
[36] Y.X. Zou, Z.K. Zhang, J.W. Yan, L.H. Lin, G.Y. Huang, Y.D. Tan, Z. You, P. Li, High-temperature flexible WSe2 photo-detectors with ultrahigh photoresponsivity, Nat Commun 13 (2022) 4372.
[37] X. Gao, J. Li, R. Du, J.Y. Zhou, M.Y. Huang, R. Liu, J. Li, Z.Q. Xie, L.Z. Wu, Z.F. Liu, J. Zhang, Direct Synthesis of Graphdiyne Nanowalls on Arbitrary Substrates and Its Application for Photoelectrochemical Water Splitting Cell, Adv Mater 29 (2017).
[38] J.Y. Zhou, X. Gao, R. Liu, Z.Q. Xie, J. Yang, S.Q. Zhang, G.M. Zhang, H.B. Liu, Y. L. Li, J. Zhang, Z.F. Liu, Synthesis of Graphdiyne Nanowalls Using Acetylenic Coupling Reaction, J Am Chem Soc 137 (2015) 7596–7599.
[39] J. Li, X. Gao, B. Liu, Q.L. Feng, X.B. Li, M.Y. Huang, Z.F. Liu, J. Zhang, C.H. Tung, L. Z. Wu, Graphdiyne: A Metal-Free Material as Hole Transfer Layer To Fabricate Quantum Dot-Sensitized Photocathodes for Hydrogen Production, J Am Chem Soc 138 (2016) 3954–3957.
[40] J.L. Wen, W.H. Tang, Z. Kang, Q.L. Liao, M.Y. Hong, J.L. Du, X.K. Zhang, H.H. Yu, H.N. Si, Z. Zhang, Y. Zhang, Direct Charge Trapping Multilevel Memory with Graphdiyne/MoS2 Van der Waals Heterostructure, Adv Sci 8 (2021).
[41] R.S. Zucker, W.G. Regehr, Short-term synaptic plasticity, Annu Rev Physiol 64 (2002) 355–405.
[42] C.H. Li, W. Du, Y.X. Huang, J.H. Zou, L.Z. Luo, S. Sun, A.O. Govorov, J. Wu, H. X. Xu, Z.M. Wang, Photonic synapses with ultralow energy consumption for artificial visual perception and brain storage, Opto-Electron Adv 5 (2022).

[43] J.G. Simmons, G.W. Taylor, Nonequilibrium Steady-State Statistics and Associated Effects for Insulators and Semiconductors Containing an Arbitraty Distribution of Traps, Phys Rev B-Solid St 4 (1971) 502.
[44] F.Q. Zhang, C.Y. Li, Z.Y. Li, L.X. Dong, J. Zhao, Recent progress in three-terminal artificial synapses based on 2D materials: from mechanisms to applications, Microsyst Nanoeng 9 (2023).
[45] J. Piotrowski, W. Gawron, Ultimate performance of infrared photodetectors and figure of merit of detector material, Infrared Phys Techn 38 (1997) 63–68.
[46] L.L. Min, Y.C. Zhou, H.X. Sun, L.Q. Guo, M. Wang, F.R. Cao, W. Tian, L. Li, Carrier dynamic identification enables wavelength and intensity sensitivity in perovskite photodetectors, Light-Sci Appl 13 (2024).
[47] Z.W. Jin, Y.H. Chen, Q. Zhou, P. Mao, H.B. Liu, J.Z. Wang, Y.L. Li, Graphdiyne for multilevel flexible organic resistive random access memory devices, Mater Chem Front 1 (2017) 1338–1341.
[48] X. Liu, S.L. Dai, W.D. Zhao, J.Y. Zhang, Z.Y. Guo, Y. Wu, Y.T. Xu, T.R. Sun, L. Li, P. Guo, J. Yang, H.W. Hu, J.H. Zhou, P. Zhou, J. Huang, All-Photolithography Fabrication of Ion-Gated Flexible Organic Transistor Array for Multimode Neuromorphic Computing, Adv Mater 36 (2024).